RESEARCH ARTICLE

Band Engineering Induced Conducting 2H-Phase MoS₂ by Pd—S—Re Sites Modification for Hydrogen Evolution Reaction

Zhaoyan Luo, Junjie Li, Yongliang Li, Duojie Wu, Lei Zhang,* Xiangzhong Ren,* Chuanxin He, Qianling Zhang, Meng Gu, and Xueliang Sun*

The electronic band structure of MoS₂ exerts far-ranging effects on the applications of these materials, ranging from chemical catalysis, electronic, and magnetic behaviors. However, the underlying relationship between the electronic band structure and activity is largely unknown in heterogeneous catalysis including the hydrogen evolution reaction, partly due to the lack of a controllable methodology to achieve desirable electronic band structures in the 2H-phase MoS₂. Herein it is demonstrated that dual dopants can engineer the band structure of MoS₂ by substituting into the adjacent Mo sites. Specifically, these constructed Pd—Re dimers bridged by sulfur (Pd—S—Re sites) introduce conducting electronic states around the Fermi level to increase the metallic characteristics of MoS₂, resulting in metallic-like behavior, which is initially semiconducting. Furthermore, the efficacy of inducing a phase conversion from 2H to metallic 1T is higher for codoping with dual dopants as compared to that for the use of a single dopant, thereby generating more intrinsically active Pd—S*—Mo sites to further increase active sites density. Ultimately, this leads to the MoS₂ catalyst showing a low overpotential of 46 mV at a current density of 10 mA cm⁻² and a high exchange current density of 1.524 mA cm⁻², along with superior operating durability.

1. Introduction

Sustainable hydrogen production using renewable-powered, low-temperature water electrolyzers is essential in the quest for fossil fuel alternatives.[1,2] The lack of cost-effective substitute catalysts for Pt has hindered scalable hydrogen production over the past decades.[2–4] Owing to their relatively low cost, natural abundance, and high intrinsic per-site hydrogen evolution reaction (HER) activity of metallic edges (ΔG_H = 0.06 eV),[5] 2D transition-metal dichalcogenides,[6] such as molybdenum disulfide (MoS_2), have attracted substantial interest as replacement catalysts for the electro-chemical generation of hydrogen from water. Despite the extensive development of MoS_2 materials, the practical viability has been severely limited by a low active-site density.[7–9] The catalytic activity of MoS_2 is localized to rare metallic edge sites, whereas the majority of the basal plane sites in MoS_2 are inert.[10–12] This is because the thermodynamically stable trigonal-prismatic (2H) phase MoS_2 is typically a semiconductor with a high bandgap of 1–2 eV. Consequently, the basal planes of MoS_2 exhibit weak hydrogen bonding (ΔG_H is ≈2 eV uphill) and poor electronic transport capacity.[11,13] A narrowing of the bandgap and an increase in the number of gap states around the Fermi level improve the hydrogen adsorption strengths of metallic octahedral (1T)-phase MoS_2 basal plane sites, in contrast to the case of semiconducting MoS_2 materials; this allows the simultaneous manipulation of active-site density and charge transfer kinetics.[14] As outlined in a recent report by Nørskov et al., the metallicity, rather than structure (2H and 1T) or composition, is the most important parameter to determine the catalytic properties for the basal planes of MoS_2.[15] In principle, rationally tuning the electronic band structures may substantially contribute to the regulation of the catalytic performance of MoS_2. Thus, a better understanding of the relationships between electronic properties and catalytic activity is the key to the design of more efficient (MoS_2-based) HER catalysts and the enhancement of catalytic activity based on the regulation of electronic band structures.

Z. Luo, Y. Li, L. Zhang, X. Ren, C. He, Q. Zhang
College of Chemistry and Environmental Engineering
Shenzhen University
Shenzhen, Guangdong 518060, P. R. China
E-mail: lei.zhang@szu.edu.cn; renxz@szu.edu.cn

Z. Luo
College of Physics and Optoelectronic Engineering
Shenzhen University
Shenzhen, Guangdong 518060, P. R. China

Z. Luo, J. Li, X. Sun
Department of Mechanical and Materials Engineering
University of Western Ontario
London, Ontario N6A 5B9, Canada
E-mail: xsun9@uwo.ca

D. Wu, M. Gu
Department of Materials Science and Engineering
Southern University of Science and 13 Technology
Shenzhen 518055, China

The prerequisite for a mechanistic analysis of the structure–activity relationship is the development of controllable methodologies that facilitate the electronic band structure engineering of MoS_2. Currently, extensive efforts have been expended on tuning the electronic band structure of MoS_2 through the metastable 1T-phase transformation, that is, using existing vapor-phase growth methods,[10,16] exfoliation strategies,[17] and atomic-scale modifications, such as via single-atom doping.[7,18] Unfortunately, the 1T phase of MoS_2 is intrinsically metastable and easily converted to the stable 2H phase, making it difficult to characterize the intrinsic properties of metastable 1T-MoS_2. The electronic band structure of 2H-MoS_2 can also be tuned via the introduction of sulfur vacancies (SVs) or applications of lattice strain. The introduction of SVs into the MoS_2 lattice induces modification of the electronic structure, thereby resulting in the formation of in-plane active sites for HER. However, the variation in the band structure owing to the application of strain or introduction of SVs[19] was insignificant, with only a slight energy shift of the Dirac point.[20,21] Another major limitation of defect-rich 2H-MoS_2 materials is their reduced stability due to the high sulfur-loss rate of defective 2H–MoS_2.[22] The single-atom doping has also been expended on tuning the electronic band structure of MoS_2. Doping heteroatoms into the MoS_2 lattice, on the one hand can overwhelmingly reform local electronic structures to effectively activate the basal plane S atoms and introduce in-plane active sites for the HER.[23] On another hand, some doped heteroatoms are capable of changing local atomic arrangement via lattice strain induction, finally resulting in vacancy defect generation or even regional phase transition.[24,25] However, such single dopant-induced band restructuring effects usually require considerable concentrations of single dopant exceeding a few atomic percent to reach the alloying level. Hence, it is still a critical challenge to develop a controllable methodology to achieve desirable electronic band structures of 2H-MoS_2 and consequently investigate the structure–activity relationship of MoS_2.

We addressed the aforementioned challenge in the present study. Here, a neighboring dual-heteroatom doping strategy was proposed to effectively tune the electronic band structures. This allowed the construction of a model system that was subsequently employed to investigate the intrinsic connection between the activity and electronic band structures of MoS_2. We chose this strategy to construct our model system for several reasons: i) this led to the design and synthesis of $Pd,M-MoS_2$ catalysts with tailored bands structures and thus established functional links between the measured HER properties and intrinsic electronic band structures of MoS_2; ii) the as-structured model system can also be employed to investigate the influence of other possible factors (including phases (2H/1T) and SVs) on the electronic band structure of MoS_2; iii) the defect-rich $Pd-MoS_2$ constructed using this strategy demonstrates better matrix stability than that of pristine MoS_2;[26] thus, catalytic stability during the HER process is ensured. In particular, the construction of Pd−S−Re sites allowed the synthesis of a unique metal-like electronic band structure on 2H MoS_2, without the assistance of phase transformation and defect introduction. This resulted in intrinsic activation of the 2H basal-plane sites. In addition, the introduction of Re lowered the formation energy of 1T-$Pd-MoS_2$. Therefore, the efficacy to induce conversion to the stable 1T phase was higher for the dual-doping strategy as compared to that for single doping (Pd), thereby generating more intrinsically active Pd−S*−Mo sites with an almost thermoneutral ΔG_H. Consequently, the fabricated $Pd,Re-MoS_2$ yields the highest HER performance achieved thus far using phase-pure MoS_2-based materials in acidic media.

2. Results and Discussion

2.1. Screening Ideal the Electronic Band Structures

Initially, the density functional theory (DFT) calculations were performed to reveal the correlation between the electronic band structure and HER activity. The ideal band structures were screened based on ΔG_H, which is known to scale with reaction activation energies.[27] The parameter has been successfully utilized as a descriptor to correlate theoretical predictions with experimental measurements of the catalytic activities for various systems,[28] including the MoS_2 materials. We previously reported the activation of the basal-plane S sites with the introduction of Pd atoms into the 1T-MoS_2 matrix. Here, the S sites in 1T-$Pd-MoS_2$ exhibited an almost thermoneutral ΔG_H of −0.02 eV.[26,29] The doping of Pd into the 2H-MoS_2 lattice exerted no significant effect on the activity modulation of MoS_2, and the corresponding ΔG_H of the basal-plane S sites in 2H-$Pd-MoS_2$ was 0.54 eV. Despite the similarities in the structure and composition, a significant difference was observed in the catalytic activity. This may be attributed to the electronic effects. Therefore, these two model materials were initially selected to investigate the relationship between the HER activity and electronic band structures of MoS_2 (**Figure 1**a and Figure S1, Supporting Information). As expected, the 2H-phase $Pd-MoS_2$ material is an indirect-bandgap semiconductor that has a bandgap of ≈1 eV.[19] By contrast, the electronic band structures of 1T-phase $Pd-MoS_2$ show highly distorted indirect bandgaps or reveal metal-like behavior with a narrowing bandgap and an increasing number of gap states around the Fermi level.[20] These behaviors are consistent throughout the Brillouin zone, as seen in each supercell density of states (DOS) shown at the right of each band-structure calculation. It was inferred that the basal plane of the 2H-$Pd-MoS_2$ surface contained active sites in the form of SVs; however, the substantial bandgap resulted in inertness for HER, thus revealing the important roles of the electronic band structures in the HER catalytic properties of MoS_2 materials. Thus, we can optimize hydrogen adsorption on active sites by narrowing the bandgap and increasing the number of gap states around the Fermi level, thus resulting in the activation of the intrinsic catalytic properties of the basal plane of 2H-phase $Pd-MoS_2$.

The electronic band structure of TMDs generally depends on the coordination environment of the transition-metal centers and the respective d-electron count;[18,30] Thus, the electronic band structure of MoS_2 may be adjusted using various heteroatom dopants (such as Re and Cr) with different d-electron counts. These dopants also have been identified as good candidates for tuning the electronic properties of TMDs,[21,24] although such single dopant-induced band restructuring effects
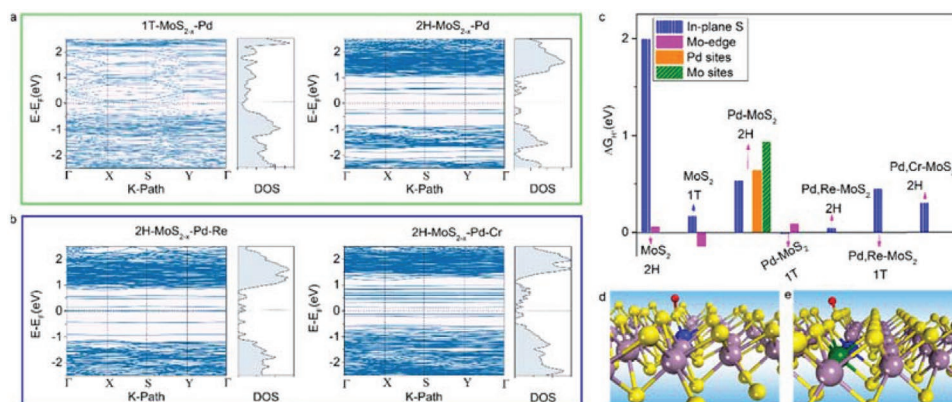
Figure 1. Theoretical calculations of the effects of electronic band structures on HER activity of MoS$_2$. a) Electronic band structures and the supercell density of states (DOS) (right) of 1T-MoS$_{2-x}$ and 2H-MoS$_{2-x}$ with single Pd dopants. b) Electronic band structures and the DOS (right) of 2H-MoS$_{2-x}$ and 2H-MoS$_{2-x}$ with Pd,Cr co-dopants. c) Free energy versus the reaction coordinates of different active sites. d) Adsorption structures of H* at the in-plane S sites of 1T Pd-MoS$_2$ and 2H Pd,Re-MoS$_2$.

usually require considerable concentrations of single dopant exceeding a few atomic percent to reach the alloying level. The influence of heteroatom (Re, Cr) doping on the band structure of 2H Pd-MoS$_2$ is summarized in Figure 1b–d and Figures S2 and S3, Supporting Information. The DFT calculations showed that the introduction of heteroatoms induced the appearance of new bands in the gap near the Fermi level. The bandgap between these new bands and the Fermi level was ordered in the following sequence: Pd-MoS$_2$ > Pd,Cr-MoS$_2$ > Pd,Re-MoS$_2$. This sequence was opposite to that for the predicted HER activity, that is, Pd-MoS$_2$ < Pd,Cr-MoS$_2$ < Pd,Re-MoS$_2$. These results suggested that tuning of the electronic band structure of MoS$_2$ was associated with the regulation of the HER activity. Dual doping using different heteroatoms, such as Pd-M, M: Re, Cr, results in different activity levels. The efficacy of synergistic tuning of ΔG_H was higher for the structures subjected to dual doping as compared to that for the structures subjected to single doping (Pd). Specifically, upon the introduction of Pd−Re dual dopants, the aforenoted new bands move close to the Fermi level, thus resulting in no bandgap and an increased number of gap states around the Fermi level, which increase the hydrogen adsorption strength of the basal S sites. The unique metal-like electronic band structure[30,31] gives rise to the optimal ΔG_H (=0.05 eV), which allows us to achieve the highest intrinsic HER activity among MoS$_2$-based catalysts. In addition, we also compared the changes in the band structure of Pd,Re-MoS$_2$ before and after the sulfur defect was introduced. The similar band structure at the Fermi level indicates that the engineering of the band structure is not due to the introduction of sulfur defects. Thus, the introduction of substitutional Re and Pd dopants can generate conducting electronic states around the Fermi level of 2H MoS$_2$, even without the assistance of phase transformation and defect introduction.

The distance between the two heteroatoms also exerted a substantial impact on the synergistic interactions. As shown in **Figure 2**a, when the doping load of metal atoms was low, the Pd and Re atoms remained distant. The synergistic interaction between the two heteroatoms was negligible. Increasing the number of heteroatoms will decrease the distance between Pd and Re, potentially leading to synergetic interactions. Upon

minimizing this distance, the Pd and Re atoms work in synergy to tune the ΔG_H values of the basal sulfur sites. In particular, dual dopants (Pd, Re) are substituted to adjacent Mo sites to form a Pd−S−Re configuration. The synergetic interaction between neighboring heteroatoms on MoS$_2$ greatly enhances HER activity of basal S sites, leading to optimal $\Delta G_H \approx 0$ eV. This synergistic interaction between neighboring Pd and Re atoms was also confirmed by Bader charge analysis (Figure 2b). The results of the Bader charge changes of S atoms revealed that the electron number on S atoms adjacent with doping heteroatom is obviously reduced. According to the molecular orbital theory (Figure 2c), when H atom is absorbed on S atom, the combination of H 1s orbital and S 3p orbital will form a bonding orbital (s) and anti-bonding orbital (s*), where the energy level matching degree of H atom and S atom determines the H−S bonding strength on basal sulfur atoms. Decreasing the electron number on S atom will balance the energy level mismatching for enhancing the H adsorption, thereby activating the inert basal plane and accelerating the HER. Especially the S sites adjacent to Pd (Pd−S*−Mo) in the 2H Pd,Re-MoS$_2$ exhibits lowest the electron density, thus yielding the optimal ΔG_H.

In addition, dual dopants are more easily induced in the formation of metallic 1T Pd-MoS$_2$ as compared to that for the use of a single dopant, thereby generating more intrinsically active Pd−S*−Mo sites[26] to further increase active sites density. This was ascribed primarily to two reasons. First, the Re−S bond energy, which is lower than the Mo−S bond energy,[19] can help introduce SVs during the subsequent interfacial MoS$_2$/Pd (II) redox reaction.[26] Second, the stability of 1T- and 2H-Pd-MoS$_2$ was inversely related to the increase in Re concentration. When the Re concentration exceeded 45%, the 1T phase became more stable than the 2H phase (Figure 2d). The resulting SVs also enabled stabilization of 1T-Pd-MoS$_2$. A variation in the doping number of metallic heteroatoms (Pd, Re) allowed manipulation of the number of SV sites and induced phase transition. Therefore, the adopted model systems were also utilized to investigate the influence of these factors, that is, phase and SVs, on the electronic band structure of MoS$_2$.
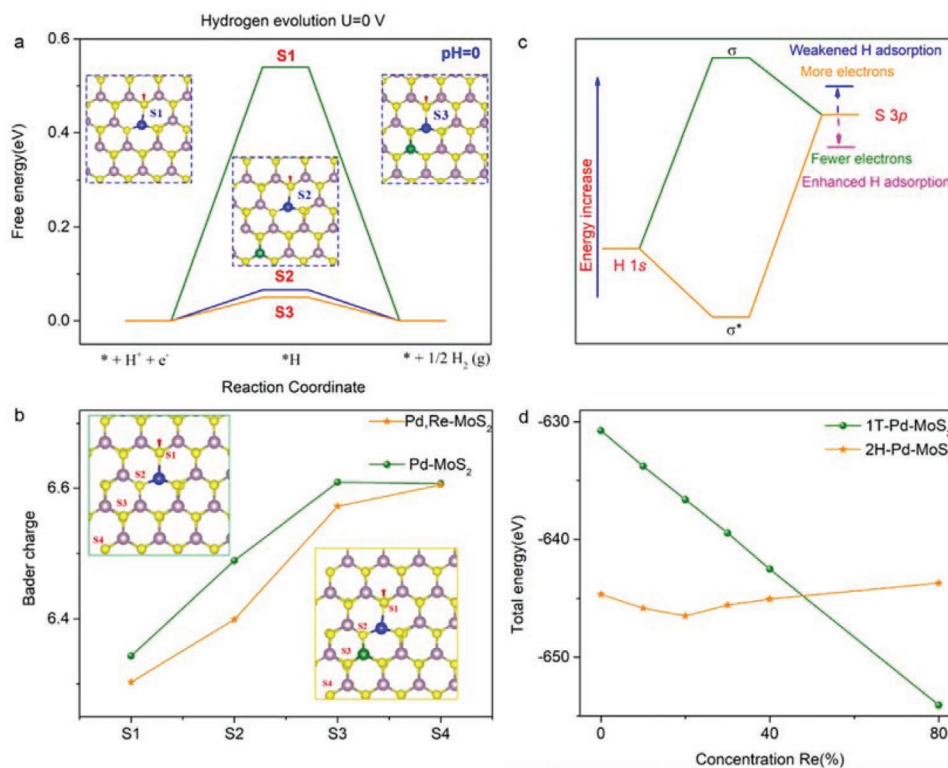
**ADVANCED
SCIENCE NEWS**
www.advancedsciencenews.com

**ADVANCED
ENERGY
MATERIALS**
www.advenergymat.de

Figure 2. DFT calculations. a) Hydrogen adsorption free energy of H* at the in-plane S sites of 2H-Pd,Re-MoS$_2$ confining two heteroatoms (Pd, Re) with different doping distances. b) Schematic diagram of the bonding of H 1s orbital and S 3p orbital (from MoS$_2$), where depletion of electrons on S atoms will lower the orbital position and enhance the H—S bond. c) Bader charge analysis of 2H-MoS$_{2-x}$ with Pd,Re co-dopants, and 2H-MoS$_{2-x}$ with single Pd dopants. d) DFT calculation for the energetics of Re doping to promote the HER activity of MoS$_2$ variation in the energy of 2H-phase Pd-MoS$_2$ and 1T-phase Pd-MoS$_2$ as the concentration of Re changes.

2.2. Synthesis and Structural Characterization

Pd,Re-MoS$_2$ was synthesized based on its predicted structure, and a detailed illustration of the synthesis procedures is provided in the Methods section. Briefly, the synthesis of Pd,Re-MoS$_2$ involved two important steps. Initially, the Re-MoS$_2$ materials were fabricated via a typical solvothermal method using $(NH_4)_6Mo_7O_{24}$ $4H_2O$, CH_4N_2S, and NH_4ReO_4 as precursors. Subsequently, the substitution of Mo with Pd atoms via spontaneous interfacial doping resulted in the formation of the desired Pd,Re-MoS$_2$ catalysts. Pd-MoS$_2$ samples with an identical Pd loading were also prepared using a similar method to facilitate comparison. The field-emission scanning electron microscopy (SEM), transmission electron microscopy (TEM) patterns and the Raman spectra (Figures S4–S6, Supporting Information) show that the morphological and structural features of Pd,Re-MoS$_2$ were similar to those of Pd-MoS$_2$ and Re-MoS$_2$ samples, which are all composed of roselike 2D nanosheets of MoS$_2$. Further, no Re-containing nanoparticles or large clusters were observed in the TEM images of the Pd,Re-MoS$_2$. This was also confirmed by the X-ray diffraction (XRD) analysis (Figure S7, Supporting Information), where diffraction peaks of Re-based crystalline phases were not detected. The crystallinity was additionally characterized using high-resolution TEM and XRD. The results revealed an interlayer distance of 0.62 nm (Figure S8, Supporting Information), which corresponded to the (002) plane of hexagonal 2H-MoS$_2$.[24] This observation was consistent with

the results of XRD analysis, which indicated the 2H-MoS$_2$ characteristics of the crystal structure of Pd,Re-MoS$_2$. High-angle annular dark-field scanning transmission electron microscopy (HAADF-STEM) and the corresponding elemental mappings demonstrated that Re and Pd were homogeneously distributed in the MoS$_2$ backbone (**Figure 3**a,b). The results from heat-treatment TEM and X-ray diffraction (XRD, Figure S9, Supporting Information) tests suggest that Pd was firmly integrated into the MoS$_2$ backbone without phase segregation even at 600 °C. Figure S10, Supporting Information, shows the atomic resolution high-resolution TEM (HRTEM) image of the Pd, Re-MoS$_2$ sample. The Pd,Re-MoS$_2$ is in 2H phase with (0 0 1) basal plane perpendicular to electron beam. The molybdenum (chalcogen) atoms in the upper layer are aligned with the chalcogen (molybdenum) atoms in the lower layer, thereby forming a hollow hexagonal structure when viewed from the c-axis direction. We can distinguish Mo atoms from S atoms from the effects of composition on image contrast. No Pd or Re atom was observed in hollow sites of 2H-MoS$_2$. Aberration-corrected HAADF-STEM images also showed an ordered MoS$_2$ crystalline structure after the introduction of Re and Pd atoms, which is evident from the atomic dispersion of Re and Pd. The heavy Re species were discernible in the MoS$_2$ matrix, and they were labeled using fuchsia circles in Figure S11, Supporting Information. The presence of bright spots indicated the homogeneous dispersion of the individual Re atoms on the MoS$_2$ backbone. It was difficult to distinguish Pd and Mo using

ADVANCED
SCIENCE NEWS

www.advancedsciencenews.com

ADVANCED
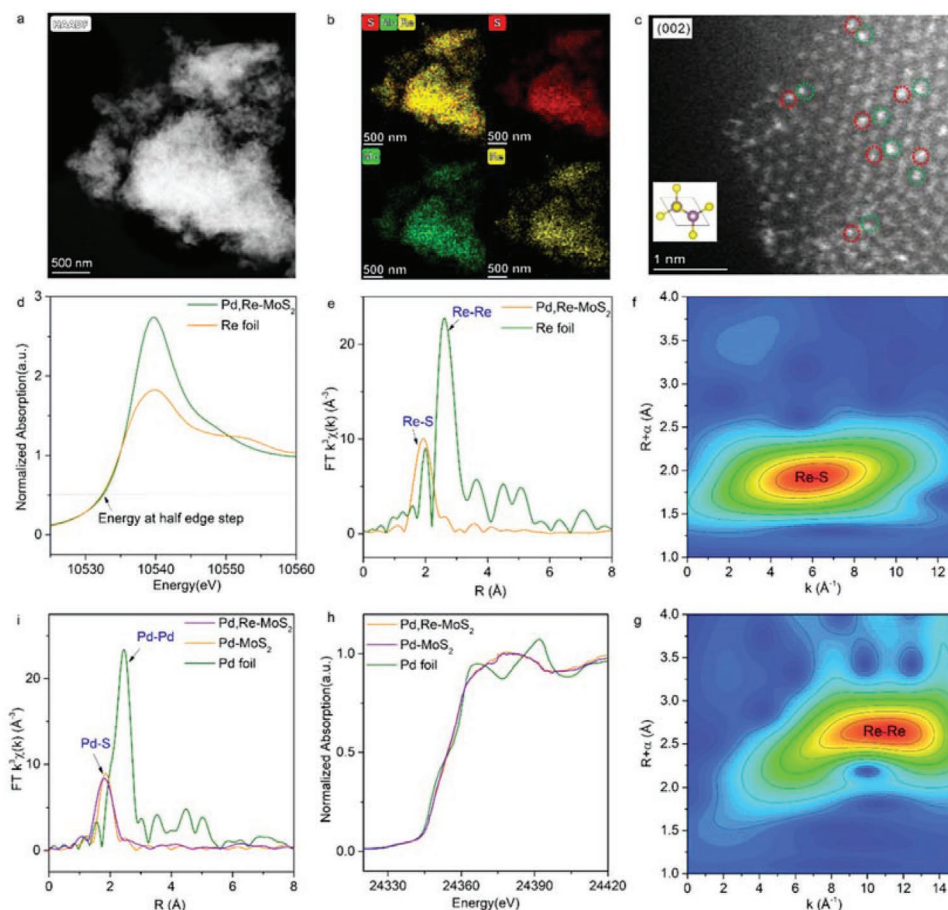**ENERGY**
MATERIALS

www.advenergymat.de

Figure 3. Structural characterization of Pd,Re-MoS₂, and Pd-MoS₂. a,b) High-angle annular dark-field scanning transmission electron microscopy (HAADF-STEM) image and corresponding EDX mappings of the Pd,Re-MoS₂. c) Atomic resolution HAADF-STEM image of Pt,Re-MoS₂. Atomic-scale HRTEM image viewed along [001] axis for MoS₂. d) Re L_3-edge XANES spectra of Pd,Re-MoS₂ and Re foil. e) Fourier transforms of the k3-weighted EXAFS data at the Re L_3-edge for Pd,Re-MoS₂, and Re foil. f) Wavelet transforms for the k2-weighted χ(k) L-edge EXAFS signals for Pd,Re-MoS₂. g) Wavelet transforms for the k2-weighted χ(k) L-edge EXAFS signals for Re foil. h) XANES spectra recorded at the Pd K-edge of Pd,Re-MoS₂, Pd-MoS₂, and Re foil. i) Fourier transform of the k3-weighted Pd K-edge of the EXAFS spectra.

sub-angstrom resolution HAADF-STEM owing to the similar Z contrasts of the two atoms. Here, we synthesized Pt,Re-MoS₂ in a similar manner to explore the presence of Pd. A series of Pt,Re-MoS₂ samples with Pt mass loadings of 2, 5, and 10% was synthesized using an identical strategy. As shown in the HAADF-STEM images of 2% Pt,Re-MoS₂ and 5% Pt,Re-MoS₂ (Figure S12, Supporting Information), Pt atoms in these samples were still atomically dispersed. An increase in the Pt mass loading in Pt,Re-MoS₂ induced a lowering of the distance between the two heteroatoms (Pt, Re) on MoS₂. As shown in the HAADF-STEM images of 5% Pt,Re-MoS₂ (Figure 3c and Figures S13 and S14, Supporting Information), we observed that the heteroatoms replaced the neighboring Mo atoms in the MoS₂ nanosheets, which support the presence of Pd—S—Re sites in MoS₂.

X-ray photoelectron spectroscopy (XPS), X-ray absorption near-edge spectroscopy (XANES), and extended X-ray absorption fine structure (EXAFS) analyses were further conducted to determine the electronic and coordination structures of Re atoms in MoS₂ catalysts. The high-resolution Re 4f spectra (Figure S15, Supporting Information), obtained via XPS,

revealed that Re was immobilized as Re (II) in MoS₂. This was confirmed by the presence of binding energy peaks at 41.783 eV (4p7/2) and 44.183 eV (4p5/2), excluding the fact that the Re species in Pd,Re-MoS₂ samples were in the metallic state. The XANES spectra (Figure 3d) reveal that the energy of half-edge-step of Pd,Re-MoS₂ is obviously higher than that of Re foil, further corroborating Re species in atomically dispersed Re-MoS₂ were oxidized. EXAFS analysis also verified the isolated dispersion of Re atoms. The Fourier-transform k3-weighted EXAFS data (Figure 3e) corresponding to the Re L_3-edge for Pd,Re-MoS₂ show the disappearance of the first-shell Re—Re scattering peak at 2.74 Å, in contrast with the data for Re foils. A dominant peak centered at a much lower R position was observed instead, and was assigned to the Re—S bond. The isolated dispersion of Re atoms in Pd,Re-MoS₂ was confirmed via high-power wavelet transform (WT) analysis. Figure 3f,g shows the WT contour plots for the three k2-weighted χ(k) signals based on Morlet wavelets with an optimal resolution. The intensity maximum presented different coordinates (k, R), whose locations were primarily associated with the path length, R, and atomic number, Z. The WT-EXAFS contour plots exhibited only a predominant

intensity maximum at ≈6 Å^{-1} for the Pd,Re-MoS$_2$ sample. The absence of a Re−Re metallic path (Re foil: ≈11 Å^{-1}) confirmed the atomic dispersion of the Re species in the MoS$_2$ matrix. The local coordination configurations of Re were investigated using the quantitative least-squares EXAFS curve-fitting analyses (Figure S16 and Table S1, Supporting Information). The optimal-fit result revealed a Re−S bond distance of 2.36 Å with a Re to S coordination number (CN) of 5.2.

XANES and EXAFS spectroscopy were performed to elucidate the electronic and coordination structures of the Pd atoms. The absorption edge of the Pd K-edge XANES spectra was located at a higher energy level for Pd,Re-MoS$_2$ as compared to that for the Pd foil, as confirmed by the Pd K-edge XANES profiles (Figure 3h and Figure S17, Supporting Information). This indicated that the Pd species were formed neither as metallic Pd nanoparticles nor as Pd clusters, which was consistent with the XPS results (Figure S18, Supporting Information). Furthermore, approximately no changes were observed in the profiles of the Pd K-edge XANES spectra for the Pd-MoS$_2$ and Pd,Re-MoS$_2$ samples, suggesting the negligible effect of Re doping on the electronic structure of Pd. This was confirmed by the results of Pd 3d XPS analysis, which revealed no discernible shift in the binding energy peaks at 336.7 (3d5/2) and 342 eV (3d3/2). The local chemical structure of Pd was further investigated by EXAFS (Figure 3i, Figure S19 and Table S2, Supporting Information). From the Fourier transform of k3-weighted Pd K-edge EXAFS spectra, the disappearance of first-shell Pd-Pd scattering peak at 2.51 Å in comparison with Pd foils indicates that Pd species are not in the form of metallic Pd nanoparticles or

clusters. A prominent peak centered at a much lower R position is observed at 1.8 Å instead, corroborating the dominance of Pd−S scattering contribution. The fitting results of the Fourier transform plot exhibit a Pd−S bond distance of 2.31 Å and a Pd to S CN of 3.6. The absence of first shell Pd-Mo scattering excludes the possibility of Pd to direct bonding with Mo, thereby confirming that Pd is not occupying S sites in MoS$_2$. The best fitting of k2-weighted Pd K-edge FT spectrum of Pd,Re-MoS$_2$ shows similar profile and fitting parameters (Pd−S bond distance at 2.31±0.01 Å and CN = 3.6±0.6) to that of Pd-MoS$_2$ (Pd−S bond distance at 2.32±0.01 Å and CN = 3.8±0.3). The similarity in the profiles and fitting parameters confirmed the negligible effect of Re doping on the coordination environment of Pd. It was concluded that the local configuration of active sites (Pd−S*−Mo) was similar for Pd,Re-MoS$_2$ and Pd-MoS$_2$.

2.3. Characterization of Electronic Band Structure Engineering

The aforementioned results confirmed that Pd,Re-MoS$_2$ materials were successfully synthesized. In this section, we will reveal the dual-dopant-induced band structures in MoS$_2$ via experimental techniques. First, Raman spectra (**Figure 4**a) were acquired to investigate the influence of the Re dopant on structural phase transitions. Pristine MoS$_2$ shows two peaks at 378 and 404 cm^{-1}, which are assigned to the 2H-phase vibrational configurations of the in-plane E2g and out-of-plane A1g modes.[10,13] New distinct peaks (at 332 and 278 cm^{-1}) appeared in the Raman spectra of Pd,Re-MoS$_2$ and Re-MoS$_2$ owing to the
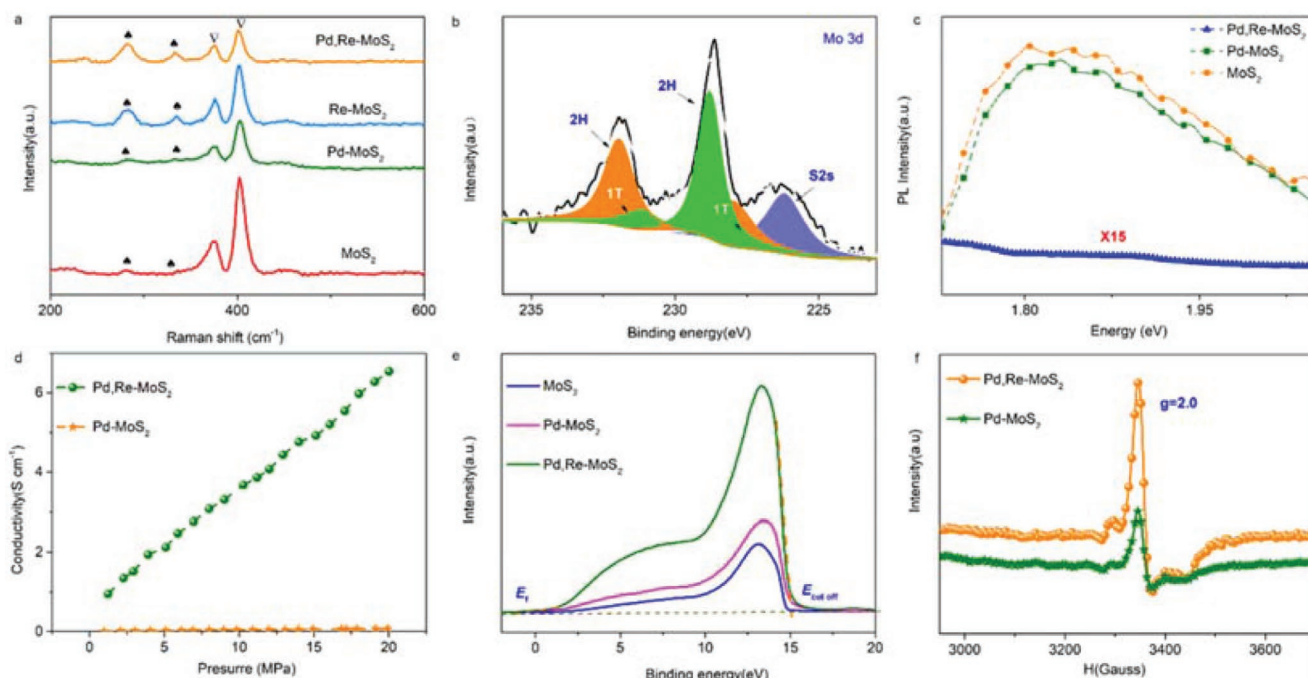

Figure 4. Characterization of electronic band structure. a) Raman spectrum. b) X-ray photoelectron spectroscopy (XPS) spectra of Mo 3d orbits of Pd,Re-MoS$_2$. c) Photoluminescence spectra of MoS$_2$, Pd-MoS$_2$, and Pd,Re-MoS$_2$. d) Conductivities of Pd-MoS$_2$ and Pd,Re-MoS$_2$ catalysts. e) Ultraviolet photoelectron spectroscopy (UPS) spectrum of MoS$_2$, Pd-MoS$_2$, and Pd,Re-MoS$_2$. f) Electron paramagnetic resonance (EPR) spectra of Pd-MoS$_2$ and Pd, Re-MoS$_2$.

**ADVANCED
SCIENCE NEWS**

www.advancedsciencenews.com

**ADVANCED
ENERGY
MATERIALS**

www.advenergymat.de

phase transformation of the MoS_2 after Re doping.[32] Our DFT calculations revealed that the band structure of 1T MoS_2 showed highly distorted indirect bandgaps and an increased number of gap states around the Fermi level. It was inferred that phase transition induced by Re doping exerted a significant effect on the band structures of MoS_2; however, the overall structural phase transition from a trigonal prismatic (2H) to an octahedral (1T) structure for Re-doped MoS_2 occurred only at a sufficiently high concentration of Re dopants, namely, at a doping percentage in the range of 40–50%.[19] These results were consistent with those obtained via Raman spectroscopy, where two primary Raman modes (A1g and E2g) were observed for the as-obtained Pd,Re-MoS_2. The concentrations of the 1T and 2H phases in Pd,Re-MoS_2 were determined using XPS analysis. The XPS spectra (Figure 4b) corresponding to the Mo 3d orbital for Pd,Re-MoS_2 also confirmed the coexistence of the 1T and 2H phases, and the deconvoluted doublets were unambiguously assigned to the 1T (3d3/2 at 231.5 eV and 3d5/2 at 228 eV) and 2H (3d3/2 at 232.05 eV and 3d5/2 at 228.9 eV) phases. The results of quantitative peak deconvolution with integrated XPS analysis revealed that the concentration of the 2H phase in Pd,Re-MoS_2 was approximately 65–70%. Interestingly, the photoluminescence (PL) spectra (Figure 4c) of 2H-phase Pd, Re-MoS_2 showed a metal-like characteristic structure. Most of the PL spectra were quenched, with no visible peak above the background, indicating the formation of a metal-like electronic band structure on Pd,Re-MoS_2. By contrast, Pd-MoS_2 is a simple n-type direct-bandgap semiconductor, wherein the PL peak shifts toward higher energies and there is no loss in peak intensity relative to that of pristine 2H-MoS_2. The macroscopic observations revealed that the electronic conductivity (Figure 4d) of Pd,Re-MoS_2 was more than one order of magnitude higher than that of Pd-MoS_2 and approached that of 1T-MoS_2 (10–100 S cm^{-1}), further demonstrating the effects of the Re dopants on the electronic properties.

Ultraviolet photoelectron spectroscopy (UPS)[33] (Figure 4e and Figure S20, Supporting Information) is the most widely used technique to monitor changes in the band structure, and can be used to observe variations in the work function. Here, the work functions of MoS_2, Pd-MoS_2, and Pd,Re-MoS_2 were estimated to be 7.13, 6.08, and 4.87 eV according to the following equation,[23,29] $\Phi = h\nu + E_{cutoff} - E_{Fermi}$. The upshift in the work functions confirmed the variations in the existing electronic band structure. In particular, the energy level of the Pd,Re-MoS_2 material matched well the reduction potential of H_2O.[23] This energy-level matching will diminish or even remove the hindrances to the HER reaction process, thus decreasing the overpotential applied for the HER. Therefore, the HER activity of MoS_2 was optimized via electronic band structure engineering.

The influence of Re doping on the formation of SVs was also examined via comparisons of Pd,Re-MoS_2 and Pd-MoS_2. Electron paramagnetic resonance (EPR) spectroscopy was performed to detect the presence of unpaired electrons on coordinatively unsaturated defective sites. A signal intensity of ≈337 mT (g = 2) indicated the concentration of basal SVs.[34] The EPR spectrum (Figure 4f) revealed that the number of exposed SVs for Pd,Re-MoS_2 (3.05 × 10^3 a.u. mg^{-1}) was 2.26-times higher than that for Pd-MoS_2 (1.35 × 10^3 a.u. mg^{-1}).

2.4. HER Performance Evaluation

To verify the role of the electronic band structures engineering in boosting the intrinsic activity, the HER performance of Pd,Re-MoS_2, with Pd and Re contents of 0.5–15 wt.% and 0–30 wt.%, respectively, was evaluated via linear sweep voltammetry (LSV) using N_2-saturated 0.5 м H_2SO_4 as the electrolyte. MoS_2, Re-MoS_2, Pd-MoS_2, and 20% Pt-C were also examined using an identical method for comparison. The obtained polarization curves are summarized in **Figure 5**a and Figure S21, Supporting Information. The Pd,Re-MoS_2 sample with 16.7% Re doping and 5% Pd doping (XPS results: a Re to Pd stoichiometry of 1:1) exhibited the highest HER activity with overpotentials of 46 mV and 130 mV to achieve current densities of 10 and 100 mA cm^{-2}, respectively. The HER activity for the sample was significantly higher than that of the Pd-MoS_2 catalyst with a Pd content of 5%. To the best of our knowledge, the performance of the Pd,Re-MoS_2 catalysts was superior to that of previously reported phase-pure MoS_2 candidates in acidic media[8,11,35] and comparable to that of state-of -the-art Pt/C catalysts (Table S3, Supporting Information). These results confirmed that the basal plane of 2H-Pd-MoS_2 could be effectively activated via Re doping. However, the variation in electrocatalytic activity owing to single doping (Re) was insignificant: The Re-MoS_2 catalyst with an overpotential of 348 mV at 10 mA cm^{-2} exhibited low HER activity that was approximately equal to the HER activity of the pure MoS_2 catalyst. This implies that the electrocatalytic activity of Pd,Re-MoS_2 does not originate from Re sites; moreover, this demonstrates the high efficacy of Pd,Re codoping in tuning the electronic band structures. Moreover, the Pd,Re-MoS_2 exhibits high turnover frequency (TOF) per active site, which surpasses most state-of-the-art MoS_2 reported (Table S4, Supporting Information). Codoping amplified the influence of single doping (Re) on the electronic band structure engineering of MoS_2, thereby optimizing the HER activity. The HER performances of the ReS_2 and Pd−ReS_2 samples were also investigated, and the results are shown in Figure S22, Supporting Information. Neither of the samples shows appreciable HER activity, further confirming that the Pd and Re sites are not the active sites in the Pd,Re-MoS_2 material, which instead entails the activation of the MoS_2 basal plane via synergistic functioning of the heteroatoms facilitated regulation of the electronic band structures of MoS_2.

The Tafel plots (Figure 5b) show that Pd,Re co-doping decreases the Tafel slope from 90 to 72 mV dec^{-1}, clearly demonstrating the superior HER kinetics of Pd,Re-MoS_2 via the Volmer–Heyrovsky mechanism.[3,36] The exchange current densities (j_0) were calculated to evaluate the intrinsic HER activity of Pd,Re-MoS_2. The results indicated that codoping effectively increased the j_0 of MoS_2. The j_0 of Pd,Re-MoS_2 was 1.524 mA cm^{-2}, which is the maximum reported till rate for MoS_2-based materials. It was significantly higher than the j_0 of Pd-MoS_2 (0.393 mA cm^{-2}) and even exceeded the j_0 of 20% Pt/C (0.921 mA cm^{-2}) under an identical loading. This confirmed that codoping with Pd and Re activated the MoS_2 basal planes, thereby optimizing the HER activity. The exceptional HER performance of the Pd,Re-MoS_2 catalyst was also confirmed based on the charge-transfer resistance (R_{ct}) derived via electrochemical impedance spectroscopy (EIS) (Figure 5c).
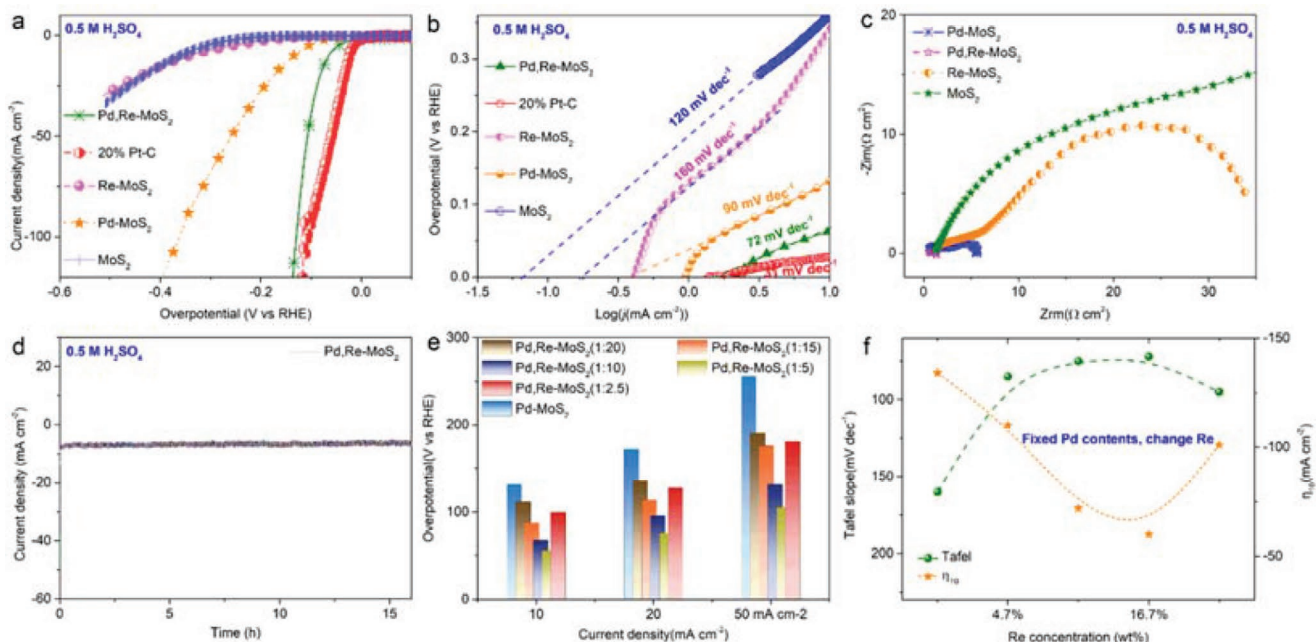
**ADVANCED
SCIENCE NEWS**
www.advancedsciencenews.com

**ADVANCED
ENERGY
MATERIALS**
www.advenergymat.de

Figure 5. HER performance evaluations. a) Linear sweep voltammetry polarization curves of Pd, Re-MoS$_2$, Pd-MoS$_2$, Re-MoS$_2$, MoS$_2$, and 20%Pt-C. b) Tafel slopes of Pd,Re-MoS$_2$, Pd-MoS$_2$, Re-MoS$_2$, MoS$_2$, and 20%Pt-C. c) Electrochemical impedance spectroscopy (EIS) Nyquist plots for Pd,Re-MoS$_2$, Pd-MoS$_2$, Re-MoS$_2$, and MoS$_2$. d) Long-time operating stability tests. e) HER polarization curves for Pd, Re-MoS$_2$ with different Re-doping contents in comparison with Pd-MoS$_2$. f) Variation trends of the Tafel slopes and η10 for different Re concentrations.

In addition to the high catalytic activity, the Pd,Re-MoS$_2$ catalysts were found to display excellent catalytic stability for the HER. The chronoamperometric test revealed the long-term working stability of the Pd,Re-MoS$_2$ catalyst beyond 100 h, without any discernible decrease in the current density (Figure 5d and Figure S23, Supporting Information). The high stability of Pd,Re-MoS$_2$ was also proved by long-term cyclic voltammetry tests, wherein a negligible potential decay was observed after 5000 cycles (Figure S24, Supporting Information). Furthermore, we conducted XPS investigations (Figure S25, Supporting Information) to examine the valance state of Re in a Pd,Re-MoS$_2$ sample after electrolysis. Neither the content nor the state of Re was altered, indicating that Re was firmly integrated into the MoS$_2$ backbone and remained highly stable under electrolytic conditions. The post XPS results and CO poisoning experiments (Figures S26 and S27, Supporting Information) of the Pd,Re-MoS$_2$ sample after electrolysis reveal that Pd is also firmly integrated into the MoS$_2$ backbone and highly stable under electrolytic conditions. It was concluded that tuning of the band structures facilitated the successful synthesis of a Pd,Re-MoS$_2$ catalyst with high activity and stability.

Although the positive effect of Pd,Re co-doping on MoS$_2$ activation was confirmed, an excessive increase in heteroatom concentrations decreased the performance (Figure 5e,f and Figure S28, Supporting Information). This was ascribed to two reasons. First, the heteroatom dopants were not the active sites in the Pd,Re-MoS$_2$ catalyst, they function by activating the MoS$_2$ basal plane via tuning of the electronic band structures and an increase in the active-site density. However, an excessively high Re content resulted in the formation of other crystal phases as well as phase separation (such as MoS$_2$/ReS$_2$), thus resulting in a decrease in the site density of Pd—S*—Mo

(1T/2H). Second, high heteroatom doping concentrations will introduce numerous SVs and simultaneously convert the 2H phase to 1T (Figure S29, Supporting Information). We found that upon conversion to high-phase-purity 1T Pd,Re-MoS$_2$, the adsorption of hydrogen on the in-plane S sites on MoS$_2$ will also become weaker (Figure S30, Supporting Information); consequently, HER was hindered. Meanwhile, the formation of the metastable 1T phase also induced a decrease in the stability during HER. The above-described results also confirm that the electronic band structure (such as metallicity), rather than structure (2H and 1T) or composition, is the most important parameter to determine the catalytic properties for the basal planes of MoS$_2$.

3. Conclusion

In summary, we have investigated the intrinsic link between the HER properties and electronic band structures for several representative MoS$_2$ models, and found that the electronic band structure plays a crucial role in the catalytic behavior of MoS$_2$. Engineering the electronic band properties at the atomic scale to induce a metal-like behavior, with a narrow bandgap and an increased number of gap states around the Fermi level, will allow favorable hydrogen adsorption on the basal-plane sites of MoS$_2$. In this work, we employed a neighboring dual-heteroatom (Pd and Re) doping strategy to successfully create a conducting electronic state around the Fermi level to increase the metallic characteristic of semiconducting 2H-MoS$_2$. Consequently, the intrinsic catalytic properties of the 2H basal plane were activated, that is, the inherent catalytic activity of the basal-plane sites was increased. In addition, codoping with Pd

and Re also stabilized metastable 1T-MoS$_2$, thereby increasing the density of 1T Pd-Mo-S* sites. The demonstrated strategy in the present study provides a new direction for the design of highly basal-plane-active MoS$_2$ electrodes, thereby facilitating the realization of the high potential of MoS$_2$ materials for HER in the future.

4. Experimental Section

Preparation of Re-MoS$_2$ Material: Re-MoS$_2$ was synthesized by a solvothermal method. First, 0.4744 g of ammonium molybdate tetrahydrate ((NH$_4$)$_6$Mo$_7$O$_{24}$.4H$_2$O), 1.0350 g thiourea (CH$_4$N$_2$S), and 0.0721g ammonium perrhenate (NH$_4$ReO$_4$) were dissolved in 30 mL water in a beaker and then sonicated for 60 min. The resulting homogenous solution was transferred to a 50 mL Teflon-lined stainless-steel autoclave and heated to 200 °C for 24 h. After cooling the solution to room temperature, the achieved precipitate was separated by centrifugation, washed with ethanol, and finally dried overnight at 50 °C.

Preparation of Pd,Re-MoS$_2$ Material: Pd,Re-MoS$_2$ was fabricated as follows: 60 mg Re-MoS$_2$ powder was mixed with 60 mL H$_2$O in a round-bottom flask, and the mixture was ultrasonicated for 1 h; then, the Pd(OAc)$_2$ solution was added to the resulting mixture followed by heating to 90 °C for 12 h. The obtained product was acquired by filtration of the suspension followed by dialysis in deionized water.

Physical Characterization: Synchrotron X-ray computed tomography was conducted at the Biomedical Imaging and Therapy (BMIT) bending magnet beamline at the Canadian Light Source (CLS). Imaging was performed using a Mo-filtered white beam with a mean incident energy of 19 keV. HAADF–STEM images were obtained using a Titan 80–300 scanning/transmission electron microscope operating at 300 kV, equipped with a probe spherical aberration corrector. The PL spectra were performed at room temperature under ambient conditions, using a 532 nm excitation laser. XPS was performed using a KratosXSAM-800 spectrometer with an Mg Kα radiation source. Binding energy was calibrated against the C 1s line. Elemental contents of the catalyst samples were determined by ICP–atomic emission spectroscopy–mass spectrometry using a Thermo Elemental IRIS Intrepid.

Electrochemical Measurements: Electrochemical performances of all catalysts were evaluated using a 750E Bipotentiostat (CH Instruments). A conventional three-electrode device was employed, comprising a saturated calomel electrode as the reference electrode, a graphite rod as the counter electrode, and a catalyst-coated glassy carbon electrode (3 mm in diameter) as the working electrode. Inks were prepared by dispersing 5 mg catalyst (Pd,Re-MoS$_2$, Re-MoS$_2$, Pd-MoS$_2$, 20 wt.% Pt/C, or ReS$_2$) in a mixture containing 50 µL Nafion (5 wt.%) solution and 950 µL ethanol under ultrasonication. The catalyst loading on the electrode was calculated to be approximately 0.354 mg cm^{-2}, and the geometric area of the glassy carbon electrode used herein was 0.07065 cm^2. HER performances were tested in N$_2$-saturated 0.5 M H$_2$SO$_4$ via LSV at a scan rate of 10 mV s^{-1}. Accelerated durability tests were conducted to investigate the stability of the catalysts by applying continuous potential cycling between 0.1 and −0.6 V versus RHE. The sweep rate was 100 mV s^{-1}. Initial and final HER LSV curves were recorded. All data presented herein were *iR*-corrected, and the solution resistances were determined by EIS. The potential values were shown with respect to RHE.

DFT Calculations: The present first principle DFT calculations were performed by Vienna Ab initio Simulation Package (VASP) with the projector augmented wave (PAW) method.[37,38] The exchange-functional was treated using the generalized gradient approximation (GGA) of Perdew–Burke–Ernzerhof (PBE) functional.[37] The energy cutoff for the plane-wave basis expansion was set to 400 eV and the force on each atom less than 0.01 eV Å^{-1} was set for convergence criterion of geometry relaxation. Grimme's D3 correction was employed to account for dispersion interaction. The Brillouin zone integration was performed using 3 × 3 × 1 Monkhorst and Pack k-point sampling through all the computational processes.[15] The self-consistent calculations applied a convergence energy threshold of 10^{-6} eV.

The free energy of the HER was calculated by the equation:[39]

$$\Delta G = \Delta E_{DFT} + \Delta E_{ZPE} - T\Delta S \tag{1}$$

where ΔE_{DFT} is the DFT electronic energy difference, ΔE_{ZPE} and ΔS are the correction of zero-point energy and the variation of entropy, respectively, which were obtained by vibration analysis, T is the temperature (T = 298.15 K). According to previous study, a correction of −0.08 eV has been used to eliminate PBE error for gas-phase H$_2$.

Supporting Information

Supporting Information is available from the Wiley Online Library or from the author.

Conflict of Interest

The authors declare no conflict of interest.

Author Contributions

X.S., L.Z., and X.R. co-supervised the whole work. Z.L., C.H., Q.Z., and Y.L. contributed to the synthesis of material and the characterization. Z.L., L.Z., X.S., X.R., and Q.Z. contributed to the analysis of the electrochemical experiments' results. Z.L. contributed to the theory calculation. J.L. and Z.L. contributed to the X-ray absorption fine structure spectroscopy. The manuscript was primarily written by Z.L., X.S., L.Z., and X.R. All authors contributed to discussions and manuscript review.

Data Availability Statement

Research data are not shared.

[1] Y. Jiao, Y. Zheng, M. Jaroniec, S. Z. Qiao, *Chem. Soc. Rev.* **2015**, 44, 2060.

[2] X. Wang, C. Xu, M. Jaroniec, Y. Zheng, S. Z. Qiao, *Nat. Commun.* **2019**, *10*, 4876.

[3] J. Dai, Y. Zhu, H. A. Tahini, Q. Lin, Y. Chen, D. Guan, C. Zhou, Z. Hu, H. J. Lin, T. S. Chan, C. T. Chen, S. C. Smith, H. Wang, W. Zhou, Z. Shao, *Nat. Commun.* **2020**, *11*, 5657.

[4] a) M. T. M. Koper, *J. Solid State Electrochem.* **2015**, *20*, 895; b) J. Staszak-Jirkovsky, C. D. Malliakas, P. P. Lopes, N. Danilovic, S. S. Kota, K. C. Chang, B. Genorio, D. Strmcnik, V. R. Stamenkovic, M. G. Kanatzidis, N. M. Markovic, *Nat. Mater.* **2016**, *15*, 197; c) H. Jin, X. Wang, C. Tang, A. Vasileff, L. Li, A. Slattery, S. Z. Qiao, *Adv. Mater.* **2021**, *33*, 2007508.

[5] a) H. Li, C. Tsai, A. L. Koh, L. Cai, A. W. Contryman, A. H. Fragapane, J. Zhao, H. S. Han, H. C. Manoharan, F. Abild-Pedersen, J. K. Norskov, X. Zheng, *Nat. Mater.* **2016**, *15*, 48; b) J. Deng, H. Li, S. Wang, D. Ding, M. Chen, C. Liu, Z. Tian, K. S. Novoselov, C. Ma, D. Deng, X. Bao, *Nat. Commun.* **2017**, *8*, 14430.

[6] H. Jin, T. Song, U. Paik, S.-Z. Qiao, *Acc. Mater. Res.* **2021**, *2*, 559.

[7] W. Wu, C. Niu, C. Wei, Y. Jia, C. Li, Q. Xu, *Angew. Chem., Int. Ed. Engl.* **2019**, *58*, 2029.

[8] H. I. Karunadasa, E. Montalvo, Y. Sun, M. Majda, J. R. Long, C. J. Chang, *Science* **2012**, *335*, 698.

[9] D. Zhu, J. Liu, Y. Zhao, Y. Zheng, S. Z. Qiao, *Small* **2019**, *15*, 1805511.

[10] S. Deng, M. Luo, C. Ai, Y. Zhang, B. Liu, L. Huang, Z. Jiang, Q. Zhang, L. Gu, S. Lin, X. Wang, L. Yu, J. Wen, J. Wang, G. Pan, X. Xia, J. Tu, *Angew. Chem., Int. Ed. Engl.* **2019**, *58*, 16289.

[11] J. Peto, T. Ollar, P. Vancso, Z. I. Popov, G. Z. Magda, G. Dobrik, C. Hwang, P. B. Sorokin, L. Tapaszto, *Nat. Chem.* **2018**, *10*, 1246.

[12] a) Y. Zhou, J. Zhang, E. Song, J. Lin, J. Zhou, K. Suenaga, W. Zhou, Z. Liu, J. Liu, J. Lou, H. J. Fan, *Nat. Commun.* **2020**, *11*, 2253; b) J. Kibsgaard, Z. Chen, B. N. Reinecke, T. F. Jaramillo, *Nat. Mater.* **2012**, *11*, 963.

[13] Q. Wang, Z. L. Zhao, S. Dong, D. He, M. J. Lawrence, S. Han, C. Cai, S. Xiang, P. Rodriguez, B. Xiang, Z. Wang, Y. Liang, M. Gu, *Nano Energy* **2018**, *53*, 458.

[14] a) X. Chen, Z. Wang, Y. Wei, X. Zhang, Q. Zhang, L. Gu, L. Zhang, N. Yang, R. Yu, *Angew. Chem., Int. Ed. Engl.* **2019**, *58*, 17621; b) A. Han, X. Zhou, X. Wang, S. Liu, Q. Xiong, Q. Zhang, L. Gu, Z. Zhuang, W. Zhang, F. Li, D. Wang, L. J. Li, Y. Li, *Nat. Commun.* **2021**, *12*, 709; c) K. Qi, X. Cui, L. Gu, S. Yu, X. Fan, M. Luo, S. Xu, N. Li, L. Zheng, Q. Zhang, J. Ma, Y. Gong, F. Lv, K. Wang, H. Huang, W. Zhang, S. Guo, W. Zheng, P. Liu, *Nat. Commun.* **2019**, *10*, 5231.

[15] C. Tsai, K. Chan, J. K. Nørskov, F. Abild-Pedersen, *Surf. Sci.* **2015**, *640*, 133.

[16] a) L. Liu, J. Wu, L. Wu, M. Ye, X. Liu, Q. Wang, S. Hou, P. Lu, L. Sun, J. Zheng, L. Xing, L. Gu, X. Jiang, L. Xie, L. Jiao, *Nat. Mater.* **2018**, *17*, 1108; b) Z. Lai, Q. He, T. H. Tran, D. V. M. Repaka, D. D. Zhou, Y. Sun, S. Xi, Y. Li, A. Chaturvedi, C. Tan, B. Chen, G. H. Nam, B. Li, C. Ling, W. Zhai, Z. Shi, D. Hu, V. Sharma, Z. Hu, Y. Chen, Z. Zhang, Y. Yu, X. Renshaw Wang, R. V. Ramanujan, Y. Ma, K. Hippalgaonkar, H. Zhang, *Nat. Mater.* **2021**, *20*, 1113.

[17] J. Chen, G. Liu, Y.-z. Zhu, M. Su, P. Yin, X.-j. Wu, Q. Lu, C. Tan, M. Zhao, Z. Liu, W. Yang, H. Li, G.-H. Nam, L. Zhang, Z. Chen, X. Huang, P. M. Radjenovic, W. Huang, Z.-q. Tian, J.-f. Li, H. Zhang, *J. Am. Chem. Soc.* **2020**, *142*, 7161.

[18] J. Suh, T. L. Tan, W. Zhao, J. Park, D. Y. Lin, T. E. Park, J. Kim, C. Jin, N. Saigal, S. Ghosh, Z. M. Wong, Y. Chen, F. Wang, W. Walukiewicz, G. Eda, J. Wu, *Nat. Commun.* **2018**, *9*, 199.

[19] X. Tian, D. S. Kim, S. Yang, C. J. Ciccarino, Y. Gong, Y. Yang, Y. Yang, B. Duschatko, Y. Yuan, P. M. Ajayan, J. C. Idrobo, P. Narang, J. Miao, *Nat. Mater.* **2020**, *19*, 867.

[20] H. Li, C. Tsai, A. L. Koh, L. Cai, A. W. Contryman, A. H. Fragapane, J. Zhao, H. S. Han, H. C. Manoharan, F. Abild-Pedersen, J. K. Norskov, X. Zheng, *Nat. Mater.* **2016**, *15*, 364.

[21] a) C. Lin, M. Ochi, R. Noguchi, K. Kuroda, A. Nomura, M. Tsubota, P. Zhang, C. Bareille, K. Kurokawa, Y. Arai, K. Kawaguchi, K. Tanaka, K. Yaji, A. Harasawa, M. Hashimoto, D. Lu, S. Shin, R. Arita, S. Tanda, T. Kondo, *Nat. Mater.* **2021**, *20*, 1093; b) P. Lu, X. Wu, W. Guo, X. C. Zeng, *Phys. Chem. Chem. Phys.* **2012**, *14*, 13035.

[22] a) Q. Li, Y. Zhao, C. Ling, S. Yuan, Q. Chen, J. Wang, *Angew. Chem., Int. Ed. Engl.* **2017**, *56*, 10501; b) K. C. Santosh, R. C. Longo, R. M. Wallace, K. Cho, *J. Appl. Phys.* **2015**, *117*, 120.

[23] Y. Shi, Y. Zhou, D. R. Yang, W. X. Xu, C. Wang, F. B. Wang, J. J. Xu, X. H. Xia, H. Y. Chen, *J. Am. Chem. Soc.* **2017**, *139*, 15479.

[24] Z. Zheng, L. Yu, M. Gao, X. Chen, W. Zhou, C. Ma, L. Wu, J. Zhu, X. Meng, J. Hu, Y. Tu, S. Wu, J. Mao, Z. Tian, D. Deng, *Nat. Commun.* **2020**, *11*, 3315.

[25] B. Pattengale, Y. Huang, X. Yan, S. Yang, S. Younan, W. Hu, Z. Li, S. Lee, X. Pan, J. Gu, J. Huang, *Nat. Commun.* **2020**, *11*, 1200.

[26] Z. Luo, Y. Ouyang, H. Zhang, M. Xiao, J. Ge, Z. Jiang, J. Wang, D. Tang, X. Cao, C. Liu, W. Xing, *Nat. Commun.* **2018**, *9*, 2120.

[27] Y. Li, X. Tan, H. Tan, H. Ren, S. Chen, W. Yang, S. C. Smith, C. Zhao, *Energy Environ. Sci.* **2020**, *13*, 1799.

[28] a) S. Li, R. Ma, Y. Pei, B. Mao, H. Lu, M. Yang, T. Thomas, D. Liu, J. Wang, *J. Phys. Chem. Lett.* **2020**, *11*, 3436; b) X. Li, Y. Fang, J. Wang, H. Fang, S. Xi, X. Zhao, D. Xu, H. Xu, W. Yu, X. Hai, C. Chen, C. Yao, H. B. Tao, A. G. R. Howe, S. J. Pennycook, B. Liu, J. Lu, C. Su, *Nat. Commun.* **2021**, *12*, 2351.

[29] Z. Luo, Y. Wang, X. Wang, Z. Jin, Z. Wu, J. Ge, C. Liu, W. Xing, *ACS Appl. Mater. Interfaces* **2019**, *11*, 39782.

[30] N. Lu, H. Guo, L. Wang, X. Wu, X. C. Zeng, *Nanoscale* **2014**, *6*, 4566.

[31] Y. Y. Liu, J. J. Wu, K. P. Hackenberg, J. Zhang, Y. M. Wang, Y. C. Yang, K. Keyshar, J. Gu, T. Ogitsu, R. Vajtai, J. Lou, P. M. Ajayan, B. C. Wood, B. I. Yakobson, *Nat. Energy* **2017**, *2*, 1.

[32] X. Zhang, Y. Liang, *Adv. Sci.* **2018**, *5*, 1700644.

[33] a) Z. Zhuang, Y. Li, Z. Li, F. Lv, Z. Lang, K. Zhao, L. Zhou, L. Moskaleva, S. Guo, L. Mai, *Angew. Chem., Int. Ed. Engl.* **2018**, *57*, 496; b) Y. Shi, Z. R. Ma, Y. Y. Xiao, Y. C. Yin, W. M. Huang, Z. C. Huang, Y. Z. Zheng, F. Y. Mu, R. Huang, G. Y. Shi, Y. Y. Sun, X. H. Xia, W. Chen, *Nat. Commun.* **2021**, *12*, 3021.

[34] a) J. Hu, L. Yu, J. Deng, Y. Wang, K. Cheng, C. Ma, Q. Zhang, W. Wen, S. Yu, Y. Pan, J. Yang, H. Ma, F. Qi, Y. Wang, Y. Zheng, M. Chen, R. Huang, S. Zhang, Z. Zhao, J. Mao, X. Meng, Q. Ji, G. Hou, X. Han, X. Bao, Y. Wang, D. Deng, *Nat. Catal.* **2021**, *4*, 242; b) G. Liu, A. W. Robertson, M. M. Li, W. C. H. Kuo, M. T. Darby, M. H. Muhieddine, Y. C. Lin, K. Suenaga, M. Stamatakis, J. H. Warner, S. C. E. Tsang, *Nat. Chem.* **2017**, *9*, 810.

[35] Y. He, P. Tang, Z. Hu, Q. He, C. Zhu, L. Wang, Q. Zeng, P. Golani, G. Gao, W. Fu, Z. Huang, C. Gao, J. Xia, X. Wang, X. Wang, C. Zhu, Q. M. Ramasse, A. Zhang, B. An, Y. Zhang, S. Marti-Sanchez, J. R. Morante, L. Wang, B. K. Tay, B. I. Yakobson, A. Trampert, H. Zhang, M. Wu, Q. J. Wang, J. Arbiol, et al., *Nat. Commun.* **2020**, *11*, 57.

[36] a) Y. Li, X. Tan, S. Chen, X. Bo, H. Ren, S. C. Smith, C. Zhao, *Angew. Chem., Int. Ed. Engl.* **2019**, *58*, 461; b) I. Ledezma-Yanez, W. D. Z. Wallace, P. Sebastián-Pascual, V. Climent, J. M. Feliu, M. T. M. Koper, *Nat. Energy* **2017**, *2*, 1.

[37] S. Kamran, K. Y. Chen, L. Chen, *Phys. Rev. B* **2009**, *79*.

[38] K. Hoshino, F. Shimojo, *J. Phys.: Condens. Matter* **1996**, *8*, 9315.

[39] Y. Li, X. Tan, R. K. Hocking, X. Bo, H. Ren, B. Johannessen, S. C. Smith, C. Zhao, *Nat. Commun.* **2020**, *11*, 2720.